

PREDICTION OF ALPINE GLACIER SLIDING INSTABILITIES: A NEW HOPE

JÉROME FAILLETTAZ, MARTIN FUNK, AND DIDIER SORNETTE

ABSTRACT. Mechanical and sliding instabilities are the two processes which may lead to breaking off events of large ice masses. Mechanical instabilities mainly affect unbalanced cold hanging glaciers. For the latter case, a prediction could be achieved based on data of surface velocities and seismic activity. The case of sliding instabilities is more problematic. This phenomenon occurs on temperate glacier tongues. Such instabilities are strongly affected by the subglacial hydrology: melt water may cause (i) a lubrication of the bed and (ii) a decrease of the effective pressure and consequently a decrease of basal friction. Available data from Allalingsletscher (Valais) indicate that the glacier tongue experienced an active phase during 2-3 weeks with enhanced basal motion in late summer in most years. In order to scrutinize in more detail the processes governing the sliding instabilities, a numerical model developed to investigate gravitational instabilities in heterogeneous media was applied to Allalingsletscher. This model enables to account for various geometric configurations, interaction between sliding and tension cracking and water flow at the bedrock. We could show that both a critical geometrical configuration of the glacier tongue and the existence of a distributed drainage network were the main causes of this catastrophic break-off. Moreover, the analysis of the modeling results diagnose the phenomenon of recoupling of the glacier to its bed as a potential new precursory sign announcing the final break-off. This model casts a gleam of hope for a better understanding of the ultimate rupture of such glacier sliding instabilities.

1. INTRODUCTION

Gravity-driven instabilities include landslides, mountain collapse, rockfalls, ice mass break-off and snow avalanches. They pose a considerable risk to mountain communities, real-estate development, tourist activities and hydropower energy generation. Gravity-driven instabilities are the most widespread natural hazard on Earth. In the US and Europe, they are particularly significant and cause billions of dollars and euros damage each year. Prediction of such gravity-driven instabilities could be used by policy makers to decide on possible evacuation of the potential dangerous area. Unfortunately, accurate prediction of such phenomena remains a challenge.

In this context, studying glacier break-off is of particular interest because a glacier consists of a unique natural material (ice) where the interface between ice and bedrock is well defined. This relative simplicity of the system allows to particularly focus our study on the rupture processes leading to the initiation of the instability. Two types of glacier instabilities leading to icefalls may be distinguished: (i) mechanical instabilities and (ii) sliding instabilities. Mechanical instabilities mainly

Key words and phrases. glacier fall, rupture, instabilities, prediction, model.

affect unbalanced cold hanging glaciers (i.e. snow accumulation is mostly compensated with break-off, *Pralong and Funk* (2006)). Based on field data combining surface displacement measurements and seismic activity before break-off, *Faillettaz et al.* (2008, 2011a) showed that a prediction of the event was possible. The case of sliding instabilities is more problematic. They occur on temperate glaciers (i.e. glaciers that can slide on their beds) where subglacial hydrology plays a major role. Melt water flowing on the glacier bed may influence the glacier dynamics in two ways: it allows (i) a better lubrication of the bed and (ii), if water becomes pressurized, an uplift decouples the glacier from its bed. In the Alps, only two glaciers are known to have given rise to such sliding instabilities in the 20th century: The glacier du Tour (Mont Blanc, France) in 1949 and the Allalingletscher (Valais, Switzerland) in 1965. Up to now, such glacier instabilities are still unpredictable, and the causes of such catastrophic break-off remain unclear.

The present paper is devoted to the study of such instabilities, taking the Allalingletscher as an example. This glacier is indeed of particular interest because it experienced 2 catastrophic break-offs (in 1965 and 2000) and also because a unique set of data was collected since the first catastrophic break-off in 1965. To address the open questions on the initiation of the instability, we apply a general numerical model developed to investigate gravity-driven instabilities in heterogeneous media. This model was already successfully applied to a polythermal glacier becoming partly temperate at its bedrock, i.e. the Altelsletscher (*Faillettaz et al.*, 2011b). Numerical results showed that the final instability is driven by a progressive cold-temperate transition at the ice/bed interface. The present study significantly differs from the previous case as here the whole glacier is temperate and can slide on its bedrock. As subglacial water was shown to drive the sliding instabilities, the initial model was extended to account for subglacial water flow at the bedrock.

After describing the Allalingletscher and analysing available measurements, we apply a general numerical model to this particular gravity-driven instability to assess the causes of the rupture. Numerical results are discussed and general criterions leading to the instability are presented.

2. ALLALINGLETSCHER

2.1. Allalingletscher through the centuries. Allalingletscher is referred to as early as 1300 in written documents, in connection with the right of pasturage. The glacier is mentioned again and again, through the centuries, mainly in reference to floods caused during stages of glacier advance, and also when it interrupted the path leading to alpine meadows and pass routes to Italy. The hydrological basin of Allalin (12 km², 81 % glacierized), located near the head of the valley of Saas, consists of a hanging valley, from which the lower part of the glacier tongue extends and flows down the sidewall of the main valley. During the little age, the terminus reached and blocked the river Saaser Vispa leading to the formation of the lake of Mattmark.

The extend of the Allalingletscher has been inferred by Lütshg (see reference in *Röthlisberger and Kasser* (1978)) from references to the size of the lake and to the floods which originated in the outburst of the ice-dammed lake. Combining such information with direct references to the size of the glacier, he assembled a detailed chronicle of the glacier through the centuries, listing large extension of the glacier in 1300 and 1589, and on other occasions during the 17th, 18th and

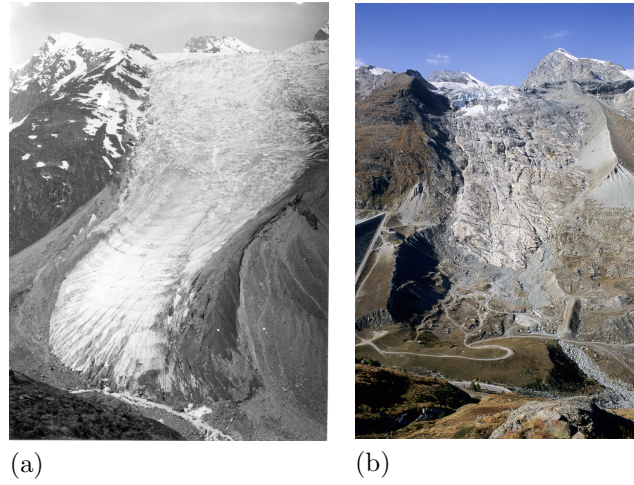


FIGURE 1. Allalingsletscher in 1916 (a) and in 2004 (b)

19th centuries. Maximum known extends occurred in 1822/1823 and 1858. The 20th century maximum in 1923 was smaller, although the terminus still crossed the main river. After that, an almost uninterrupted retreat lasting 31 years from 1923 (Fig. 1) until 1954 occurred. According to the records published in *Glaciological reports* (1881-2009), the retreat amounted to about 230 m from 1923 to 1943, 660m from 1943 to 1949, and 90m from 1949 to 1954. The very rapid retreat in the forties was due to the decay of the thinned-down snout on the east-facing rock slope of the lower part of the Saas valley sidewall. Between 1954 and 1964 the terminus has been approximately stationary (Fig. 2).

The flat area upstream the south lateral morain was used for the construction of an artificial reservoir. Between 1958 and 1967 an earth dam 120m high with a volume of 10^7m^3 was erected immediately upstream the south of the moraine. A major part of the material used in the construction of the dam was obtained from the lateral moraines, while the flat area between the moraines was used for temporary installations, primary in connection with the processing of the earth-fill materials.

2.2. The ice avalanche of 30 August 1965. The Allalin ice avalanche, a landslide-type event, is also referenced to as the Mattmark glacier catastrophe. Approximately $2 \cdot 10^6\text{m}^3$ of ice broke off at the terminus of Allalingsletscher, moved down a rock slope of some 27° over the vertical distance of 400 m and continued for a further 400 m across the flat bottom of the valley, claiming 88 victims at the Mattmark construction site. An overall view of the area shortly after the avalanche is given in Fig. 3.

Glaciological investigations showed that the ice avalanche has occurred during a phase of enhanced basal motion as a result of intensive bed-slip of an even larger mass than the one that broke off on August 30th (*Röthlisberger and Kasser, 1978*). Although it seemed that this particular condition was necessary for the lower part of the ice mass to slide off, it does not explain why the ice avalanche occurred in 1965 and not during other active phases either before or after this date. A certain

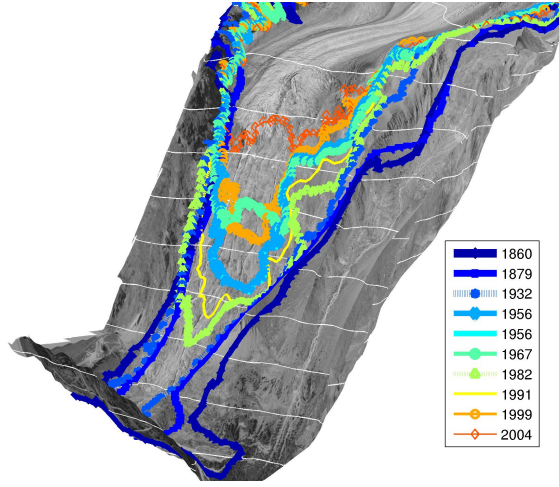


FIGURE 2. Digital Elevation Model and different extensions of the glacier tongue since 1860.



FIGURE 3. The Mattmark catastrophe: 30 August 1965 Breaking off of 2 mio m³ of ice

topography of the bed, combined with an unfortunate mass distribution, is believed to have played a major role in the catastrophe.

In terms of glacier variations, the avalanche results in a sudden retreat of the terminus by 400 m in plan view and 220 m in elevation. The avalanche deposit was not counted as part of the glacier in this context, although it took more than a year for the last remnants of the debris to melt completely. The new terminus consisted of a 40 m high ice cliff in the form of a concave crescent-shape arch.

2.3. Glaciological investigations after the ice avalanche (1965-1978) after Röthlisberger and Kasser (1978). An intensive glaciological study was undertaken immediately after the catastrophe in order to safeguard the rescue operation, and also the construction work when it was resumed later on. Since the termination of the construction of the dam in 1967 a reduced program of measurements has been carried out.

One of the methods of investigation consisted of aerial surveys repeated at short intervals of duration between one to two weeks. The first flight was carried out on 4 September, i.e. 5 days after the fall of the avalanche.

A detailed monitoring of surface velocities was carried out by means of a theodolite from the rock ridge of Schwarzbergkopf at the south side of the glacier and stakes

drilled in the ice fall. One of the practical difficulties was the installation of stable survey markers on this steep and highly crevassed glacier tongue.

Above the starting zone of the ice avalanche of 1965, a section of medium steepness remained downstream the flat upper part of the tongue. It consisted of two parts, namely an ice-fall with towering seracs separated by deep crevasses followed by a detached ice mass which did not fall down. This remaining ice mass experienced enhanced motion revealed by several features. Firstly, the ice mass was separated from the glacier by a crescent-shaped depression full of shattered ice. Secondly, numerous sharp-edged, obviously fresh crevasses cut the inner part of the mass involved, which further was more intensely shattered along one edge of the glacier. Thirdly, the talus at the foot of the glacier front was pushed over the edge of a terrasse, a clear sign that the ice cliff was undergoing rapid advance.

In the photographs of the construction site with the Allalingletscher in the background it no fresh crevasses could be observed on August 5 but, by August 30, clear ones already existed. This indicates that the catastrophic event occurred during a phase of enhanced motion, called active phase.

One of the most striking facts illustrated by Fig. 4 is that the timing of the beginning of the active phase was different each year, although its end occurred at the same time in 1965 and 1966. In 1965 the velocity was already fairly high, although still rising, when the survey started. At the beginning of November 1966, the velocity record was interrupted when the work on the dam was stopped because of the high surface velocity; most markers had disappeared when the observations were resumed at the end of the month. In 1967 the survey was discontinued before the active phase ceased completely, but the velocity records of the three years nevertheless gives a unique picture of the active phase. A common feature in the different years is a regular increase and decrease of velocity with time. The regularity of the velocity increase is particularly interesting, since a similar pattern has been observed on other glaciers prior to the breaking-off of a large ice masses; it is noteworthy, however, that the active phases ceased suddenly without formation of any major avalanches similar to that of 1965.

2.4. Glaciological survey since 1978. After the intensive glaciological surveys performed by *Röthlisberger and Kasser* (1978) after the 1965 event up to 1978, aerial surveys were performed each year. Complete stereophotogrammetry surveys were also performed in 10 years interval to generate a Digital Elevation Model of the glacier surface topography with 25 m of mesh grid (Fig. 5). Moreover, stereophotogrammetry surveys were performed every year since 1988 to investigate the ice thickness change of the glacier tongue along four different flow lines (see Fig. 6). Mass balance of Allalingletscher was reconstructed with the model GERM (Glacier Evolution Runoff Model) developed by *Huss et al.* (2010). An enhanced version of this model developed by *Farinotti et al.* (2011) was used to determine daily runoff for Allalingletscher catchment.

Thanks to available comprehensive database, it was possible to investigate the geometrical evolution of the glacier tongue, which is shown in Fig. 7(a). According to this figure, the glacier readvanced rapidly after 1965 and recovered its previous geometry 5 year later. The glacier continued to advance up to 1984. Since then, the glacier retreated, with an accelerating rate after 1997.

In August 2000, the glacier configuration was similar to 1965, and for security reasons the hazard zone was closed during summer. An ice volume of 1 Million

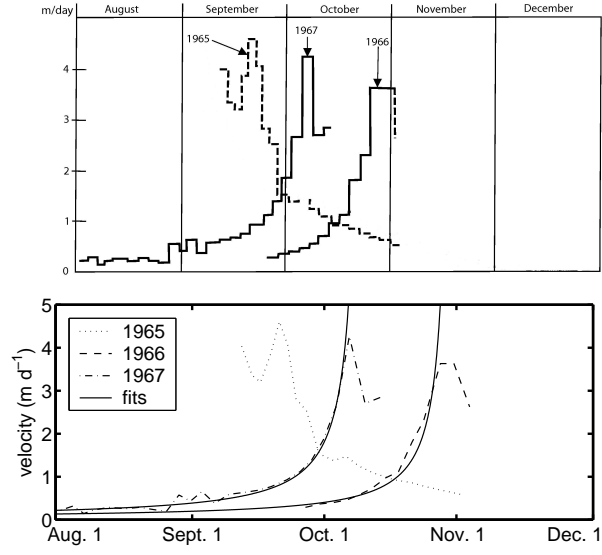


FIGURE 4. Evolution of the surface velocity of Allalingletscher tongue between 1965 and 1967.

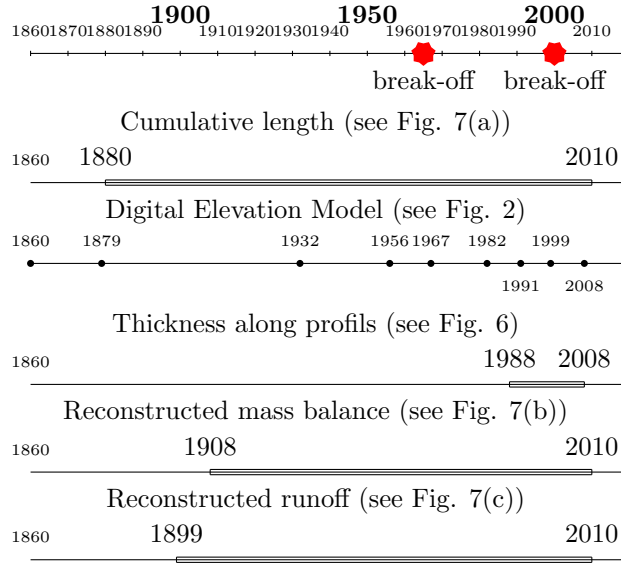


FIGURE 5. Timeline of the available data

cubic meters broke of, but did not cause any damage (Fig. 8). After this event, the glacier was stable, and the terminus stayed more or less at the same altitude.

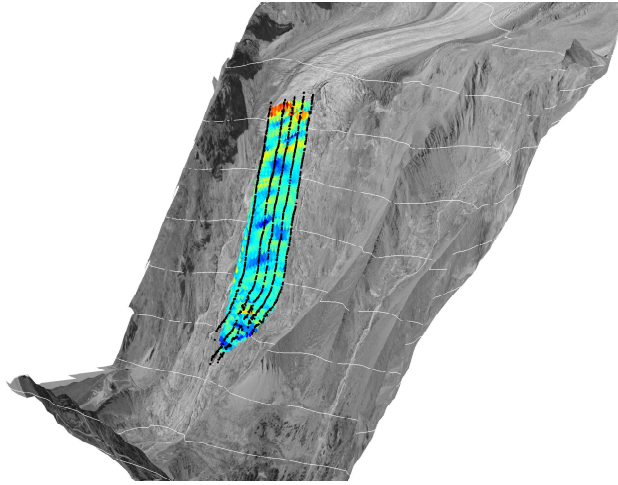


FIGURE 6. Profiles along which glacier thickness was evaluated.

2.5. Initiation of active phases. Seasonal changes in surface velocity have been observed in the years after the catastrophe, and it is now known that Allalingletscher speeded up regularly every 1-3 years, usually during summer or late autumn. In most cases no large release of ice occurred. Apparently the active phase is **necessary but not sufficient** to cause breaking off.

Figs. 7 also emphasizes the years when active phases were observed (red dots). At a first glance, they seem to appear when large rate of change of the tongue geometry occur, as they are concentrated between 1965 and 1980 (during advance) and between 1994 and 2000 (during retreat). However, no clear correlation could be found, suggesting another initiation process. The active phase has always begun during the melt season, and, perhaps even more significantly, has stopped at the beginning of the winter. This seems to indicate that meltwater plays a major role in the processes triggering the active phases. However, the initiation of such phenomenon does not seem to be correlated with the total amount of water flowing each year under the glacier (Fig. 7(c)).

Ice thickness changes at the tongue was analyzed every year since 1990 by interpolating the measured thicknesses along the 4 profiles given in Fig. 6. Fig. 9 shows the difference in tongue thickness from one year to the next.

Fig. 7(a) shows that, during this period, active phases occurred in 1994, 1996, 1997, 1998 and 1999. Interestingly, between 1990 and 1993, the geometrical extension of the glacier tongue was stable and the thickness of the tongue experienced a small homogeneous thinning. No active phases were detected during this period. Then, in 1993, the glacier started a progressive retreat and a thickening of the upper part of the tongue could be observed. This initial "pulse" is due to the positive mass balance in 1993 (Fig. 7(b)). In 1994, the tongue became thinner in the upper part while a thickening was observed behind the terminus. An active phase was detected in 1994. Since then, a "oscillating behavior" was initiated, where ice mass is first accumulated in the upper part of the tongue and then transferred to its terminus the following year. Such oscillating behavior and active phases seems to be correlated.

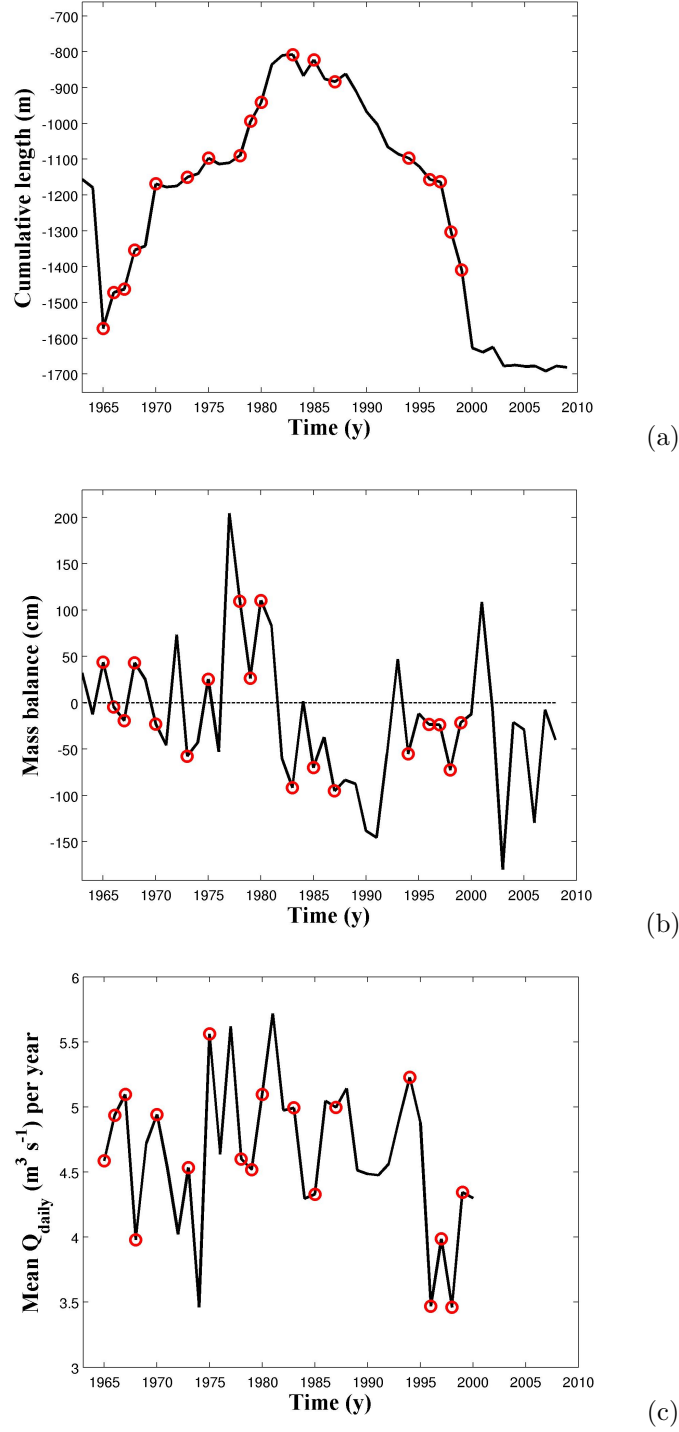


FIGURE 7. (a) Cumulative length change of Allalingletscher since 1880. Red dots indicate when active phases occurred. (b) Reconstructed mass balances since 1965. (c) Evolution of the mean daily runoff of subglacial water flow per each year.

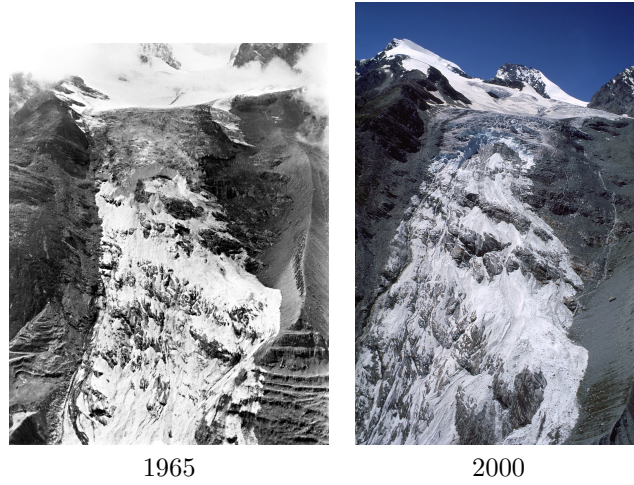


FIGURE 8. Allalingsletscher after the 1965 event (2 mio m³ of ice on August 30, 1965) and after the 2000 event (1 mio m³ on July 31, 2000)

2.6. Summary of the Allalingsletscher break-off.

- (1) There are two known events: 31.8.1965 and 31.7.2000.
- (2) The glacier tongue is **temperate**: the glacier is sliding on its bedrock.
- (3) A regular speed up of the glacier tongue during 2-3 weeks has been observed almost every year after 1965 between July and October.
- (4) Subglacial hydrology plays a major role on the instability.
- (5) The speed up of the glacier tongue is only a **necessary condition** for the breaking off.
- (6) A critical mass distribution within the glacier tongue is probably a key factor for the instability.

To investigate in more details the causes of this instability, we reanalysed this event by applying a new numerical model designed for describing natural gravity-driven instabilities (*Faillettaz et al.*, 2010). This model allows us to test the different hypothesis proposed previously to explore the possible causes of the break-off of this glacier.

3. NUMERICAL MODELING

3.1. Model description. We use a model describing the progressive maturation of a mass towards a gravity-driven instability, which combines basal sliding and cracking. Our hypothesis is that gravity-driven ruptures in natural heterogeneous materials are characterized by a common triggering mechanism resulting from a competition between frictional sliding and tension cracking. Heterogeneity of material properties and dynamical interaction of damage and cracks along the sliding layer seem to have a significant influence on the global behavior and have to be modeled.

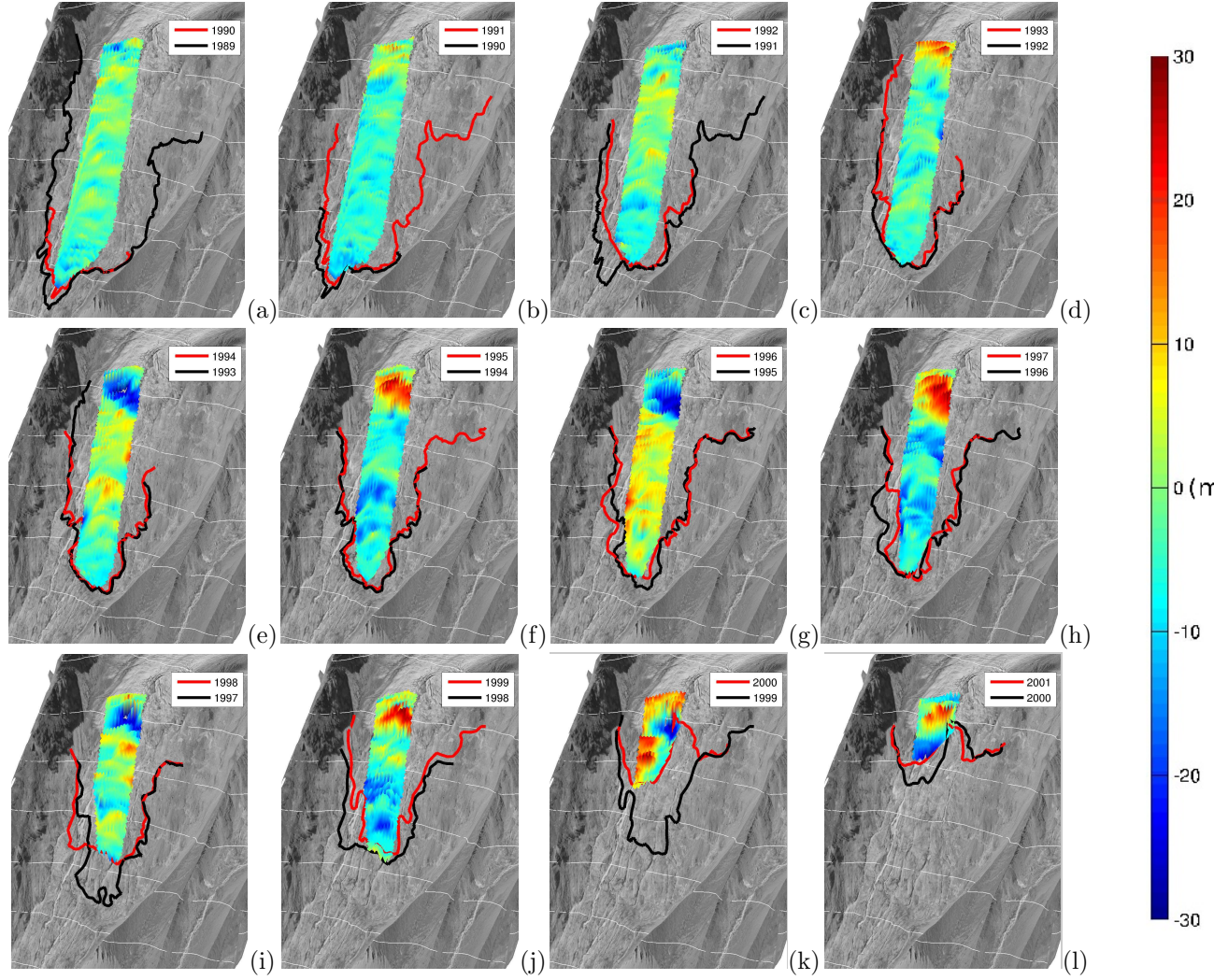


FIGURE 9. Difference of thickness of the glacier tongue between two successive years from 1989 to 2000. Spatial extension of the tongue is also shown.

This numerical model is based on the discretization of the natural medium in terms of blocks and springs forming a two-dimensional network sliding on an inclined plane (Fig. 10). Each block, which can slide, is connected to its four neighbors by springs that can fail, depending on the history of displacements and damage. We develop physically realistic models describing the frictional sliding of the blocks on the supporting surface and the tensile failure of the springs between blocks proxying for crack opening. Frictional sliding is modeled with a state-and-velocity weakening friction law with threshold. This means that solid friction is not used as a parameter but as a process evolving with the concentration of deformation and properties of sliding interfaces. Crack formation is modeled with a time-dependent

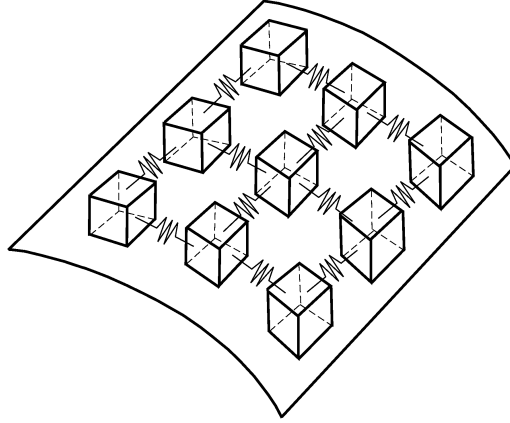


FIGURE 10. Illustration of the model consisting of spring-blocks resting on an inclined plane. The blocks lie on an inclined curved surface and gravity is the driving force. Only a small subset of the spring-block system is shown here.

cumulative damage law with thermal activation including stress corrosion. In order to reproduce cracking and dynamical effects, all equations of motion (including inertia) for each block are solved simultaneously.

The present model improves the multi-block model of *Andersen et al.* (1997) and *Leung and Andersen* (1997) in two ways. First, we use a state-and-velocity weakening friction law instead of a constant (or just state- or velocity-weakening) solid friction coefficient. Second, rather than a static threshold for the spring failures, we model the progressive damage accumulation via stress corrosion and other thermally activated processes aided by stress. Both improvements make the numerical simulations significantly longer but present the advantage of embodying rather well the known empirical phenomenology of sliding and damage processes. Adding the state and velocity-dependent friction law and time-dependent damage processes allows us to model rather faithfully the interplay between sliding and cracking between blocks and the overall self-organizing of the system of blocks (*Faillottaz et al.*, 2010).

The geometry of the system of blocks interacting via springs and with a basal surface is depicted in Figure 10. To sum up, the model includes the following characteristics:

- (1) Frictional sliding on the ground,
- (2) Heterogeneity of basal properties,
- (3) Possible tension rupture by accumulation of damage,
- (4) Dynamical interactions between blocks along the sliding layer,
- (5) Geometry and boundary conditions, and
- (6) Interplay between frictional sliding and cracking.

We describe the two key processes in the model, the friction and damage laws, that are applied to blocks and bonds respectively.

3.2. Friction law between the discrete blocks and the basal surface (after *Faillettaz et al. (2011b)*). Guided by the rate-state friction character of rock (*Dieterich, 1994*) and ice (*Fortt and Schulson, 2009; Lishman et al., 2011*), a rate- and state-dependent friction law seems also to be adequate to describe ice-bedrock friction. The version of the rate/state-variable constitutive law, currently most accepted as being in reasonable agreement with experimental data on solid friction, is known as the Dieterich-Ruina law *Dieterich (1994)*:

$$(3.1) \quad \mu(\dot{\delta}, \theta) = \mu_0 + A \ln \frac{\dot{\delta}}{\dot{\delta}_0} + B \ln \frac{\theta}{\theta_0} ,$$

where the state variable θ is usually interpreted as the proportional to the surface of contact between asperities of the two surfaces. The constant μ_0 is the friction coefficient for a sliding velocity $\dot{\delta}_0$ and a state variable θ_0 . A and B are coefficients depending on material properties.

The time evolution of the state variable θ is described by

$$(3.2) \quad \frac{d\theta}{dt} = 1 - \frac{\theta \dot{\delta}}{D_c} ,$$

where D_c is a characteristic slip distance, usually interpreted as the typical size of asperities. The friction law (3.1) with (3.2) accounts for the fundamental properties of a broad range of surfaces in contact, namely that they strengthen (age) logarithmically when aging at rest, and tend to weaken (rejuvenate) when sliding.

The primary parameter that determines stability, $A - B$, is a material property. Physically, $A - B$ indicates the sensitivity of the friction coefficient to velocity change: a negative value indicates velocity-weakening leading to an unstable slip; a positive value indicates velocity-strengthening leading to a stable slip. *Faillettaz et al. (2010)* showed that the case $A = B$ is of special interest because it retrieves the main qualitative features of the two classes, and also because, empirically, A is very close to B . Assuming $A = B$ is therefore reasonable and ensures more robust results. In Appendix A we present how the equation for the critical time t_f was obtained. t_f indicates the transition from a subcritical sliding to the dynamical inertial sliding. It is given in this case (*Faillettaz et al., 2010*) by

$$(3.3) \quad t_f = \frac{\theta_0}{\exp(\frac{\mu - \mu_0}{A}) - 1} ,$$

for $\mu > \mu_0$; Note that $t_f \rightarrow \infty$ for $\mu \leq \mu_0$, where t_f is the time when the block starts sliding, μ_0 is a constant friction coefficient, A is a constant parameter depending on material properties and θ_0 is the state parameter at steady state. The parameter μ is evaluated for each block with the definition of the solid friction $\mu = \frac{T}{N}$ where T is the tangential force determined from the position of its connected neighbors and N is the normal component of the weight of the block. The state parameter θ_0 in Eq. 3.3 is given (see Appendix A) by

$$(3.4) \quad \theta_0 = \frac{D_c}{\dot{\delta}_0} ,$$

where $\dot{\delta}_0$ is generally interpreted as the initial low velocity of a sliding mass before it starts to accelerate towards its dynamical instability and D_c can be interpreted as a characteristic slip distance over which different asperities come in contact.

Three parameters have to be correctly evaluated to model the frictional processes within the glacier: μ_0 , A and θ_0 .

An increasing friction coefficient with increasing sliding velocity (velocity-strengthening) at low velocities has been observed for polished ice-on-ice (*Kennedy et al.*, 2000; *Montagnat and Schulson*, 2003), ice-on-granite (*Barnes et al.*, 1971) and ice-on-ice along Coulombic fault (*Fortt and Schulson*, 2009). A decreasing friction coefficient with increasing sliding velocity (velocity-weakening) at high velocities has been observed as well (*Barnes et al.*, 1971; *Kennedy et al.*, 2000). The transition between these two regimes occurs at a velocity of 10^{-5}ms^{-1} (*Fortt and Schulson*, 2009). These two different behaviors are generally explained by two physical mechanisms depending on the sliding velocity regimes:

- (i) The first mechanism is the water lubrication mechanism (produced by frictional heat at the sliding surface) working at sliding velocities above roughly 0.01 m s^{-1} . The water lubrication mechanism is characterized by the low viscous resistance of a water film produced by frictional heat at the sliding interface (*Maeno and Arakawa*, 2004; *Barnes et al.*, 1971; *Kennedy et al.*, 2000; *Montagnat and Schulson*, 2003).
- (ii) The second mechanism is the adhesion and plastic deformation of ice at the friction interface, which is present at velocities lower than roughly 0.01 m s^{-1} (*Kennedy et al.*, 2000; *Montagnat and Schulson*, 2003; *Maeno and Arakawa*, 2004).

By analogy with rock physics, a rate- and state-dependent friction model for fresh and sea ice was proposed recently (*Fortt and Schulson*, 2009; *Lishman et al.*, 2011). Such a model enables to explain the change in the friction coefficient when varying sliding velocity along Coulombic shear fault or slip history. The experiments performed by *Fortt and Schulson* (2009) at -10°C on sliding along Coulombic shear faults in ice suggests that the ice-ice friction coefficient is velocity-dependent and varies between 0.6 to 1.4 depending on the applied sliding velocity along the fault. As these last results are the closest to our case, we used a mean value of $\mu_o^{\text{ice-ice}}$ equal to 0.8 in our calculation.

Once the block slides, the dynamics is controlled by a kinetic friction coefficient, which is in general smaller than the static coefficient $\mu_o^{\text{ice-ice}}$. For low temperatures, *Kennedy et al.* (2000) and *Fortt and Schulson* (2009) found a relatively constant friction coefficient around 0.6 for sliding velocities below 10^{-4}ms^{-1} , and rapidly decreasing values down to 0.1 at velocities above 10^{-4}ms^{-1} . Because velocities above 10^{-4}ms^{-1} are not expected in our model describing the nucleation phase to the catastrophic rupture, we thus assume a kinetic friction coefficient $\mu_d = 0.6$.

Next, we turn to the evaluation of the coefficient A (and B since we have made the simplifying assumption that $B = A$) in the rate- and state-dependent friction law (Eq. 3.1). Laboratory experiments suggest that A is smaller than μ_0 by typically one and sometimes up to two orders of magnitude for rock (*Ohmura and Kawamura*, 2007; *Scholz*, 2002, 1998), ranging from 0.01 to 0.2. A recent experiment on saline ice suggests however that A could be significantly higher for ice (i.e. $A \approx 0.3$) (*Lishman et al.*, 2011). As we do not have access to strong experimental constraints and since the friction law should be valid for the ice-ice and the ice-bedrock friction,

we choose $A \approx 0.1$, corresponding to one-tenth of the static friction coefficient, which is the upper limit given by *Ohmura and Kawamura* (2007) for rock.

The last parameter to be determined is θ_0 in Eq. 3.4. In the case of a glacier, the sliding velocity is typically of the order of centimeters per day. Therefore a roughly correct estimation is $\dot{\delta}_0 \approx 1 \text{ cm.d}^{-1}$. D_c can be interpreted as a characteristic slip distance over which different asperities come in contact. It is difficult to evaluate this value. The recent seismological literature reports D_c to lie in the range of tens of centimeters to meters for earthquakes (*Mikumo et al.*, 2003; *Zhang et al.*, 2003). We arbitrarily choose $D_c \simeq 1 \text{ m}$. Finally, inserting this value in equation (3.4), we obtain $\theta_0 = 100 \text{ days}$.

To account for the heterogeneity and roughness of the sliding surface, the state variable θ_i is reset to a new random value after the dynamical sliding stops. This random value should not be chosen too low in order to prevent a block which just stopped sliding from switching immediately in a new dynamical phase (i.e. $t_f = 0$). Thus, we assign $\theta_i = \nu \cdot \theta_0$ with ν uniformly distributed between 0.5 and 1.5.

Finally, the possible water lubrication of the bedrock leading to a progressive decrease of the ice-rock frictional resistance is modeled using a progressive decrease of the friction coefficient μ_0 at the interface between the simulated ice block and the basal surface (see section 3.5).

3.3. Creep law. As explained in section 3.1, bonds are modeled as linear springs in parallel with an Eyring dashpot. The springs transmit the forces associated with the relative displacements of the blocks. The spring stiffness has also to be evaluated in order to reflect the elastic property of the bulk ice mass. In continuous elasticity, Hooke's law of elasticity relates stress σ and strain ϵ via Young's modulus E : $\sigma = E\epsilon$. This leads to the expression: $\sigma_{bulk} = E_{ice} \frac{\delta L}{L}$. This stress is applied to a side surface of the block $S = L \times H$ (where H corresponds to the height and L the length of the surface), leading to an equivalent force in the bulk equal to $F_{bulk} = E_{ice} \frac{\delta L}{L} S$. A linear spring is subjected to forces given by $F_{bond} = K_{bond} \delta L$. In order to find an equivalent behavior, these two forces have to be of the same order, leading to a spring stiffness given by $K_{bond} = E_{ice} H$. Usually, values for E_{ice} are reported to be 9 GPa (*Petrovic*, 2003; *Petrenko and Whitworth*, 1999). However, there is a disagreement of an order of magnitude between measurements of E in laboratory (9 GPa) and from field observation ($\approx 1 \text{ GPa}$) as argued by *Vaughan* (1995).

Depending on the applied stress and the time scale of interest, ice has either a linear viscous or a non-linear viscous behavior. In glaciers, ice creep is usually described with a non-linear viscous rheology called Glen's flow law (see *Hutter* (1983) and references therein). This law relates, in steady-state conditions, strain rate and stress in the secondary creep regime. It is thus not possible with this law to describe the tertiary creep and the rupture of a bond. However, *Hutter* (1983) states that the so-called Prandtl-Eyring flow model shows a compatible behavior with Glen's flow law at low stresses. Non-linear viscous behavior is introduced in our model with an Eyring dashpot in parallel with a linear spring of stiffness E (which is analogous to the Prandtl-Eyring flow model), following *Nechad et al.* (2005). Its deformation e is governed by the Eyring dashpot dynamics and reads

$$(3.5) \quad \frac{de}{dt} = K \sinh(\beta s_{\text{dashpot}}),$$

where the stress s_{dashpot} in the dashpot is given by

$$(3.6) \quad s_{\text{dashpot}} = \frac{s}{1 - P(e)} - Ee .$$

Here, s is the total stress applied to the bond and $P(e)$ is the damage accumulated within the bond during its history leading to a cumulative deformation e . $P(e)$ can be equivalently interpreted as the fraction of representative elements within the bond which have broken, so that the applied stress s is supported by the fraction $1 - P(e)$ of unbroken elements. Following *Nechad et al.* (2005), we postulate the following dependence of the damage $P(e)$ on the deformation e :

$$(3.7) \quad P(e) = 1 - \left(\frac{e_{01}}{e + e_{02}} \right)^\xi ,$$

where e_{01}, e_{02} and ξ are constitutive properties of the bond material.

Finally, by combining the previous equations, *Faillietaz et al.* (2010) ended up with a creep model that computes the critical time (i.e. failure of the bond) as a function of the stress experienced by the bond s given by:

$$(3.8) \quad t_c = \begin{cases} \frac{1}{K} \exp(-\gamma s) & \text{if } s > s^* \\ \rightarrow \infty & \text{if } s \leq s^* \end{cases}$$

where

$$(3.9) \quad \gamma = \frac{\beta e_{02}^\xi}{e_{01}^\xi},$$

and

$$(3.10) \quad s^* = E \left(\frac{e_{01}}{\xi} \right)^\xi \left(\frac{\xi - 1}{e_{02}} \right)^{\xi-1} .$$

Creep properties are defined by the parameters K , β , e_{01} , e_{02} and ξ , that we need to fix for our simulations.

We need to find the most appropriate parameters to describe creep behavior of ice. The ice of natural glaciers has a complex polycrystalline structure composed of crystals of different sizes. As Equation 3.7 shows, a fraction $1 - (e_{01}/e_{02})^\xi$ of all present representative elements undergo abrupt failure immediately after the stress is applied. Since ice does not show significant damage immediately after being loaded, a reasonable assumption is $e_{01} = e_{02}$. The relative heterogeneity of the material is introduced with the parameter ξ . Despite its complex structure, ice is a fairly homogeneous material compared to fiber matrix composite. The more homogenous a material, the greater ξ . In the following, we set $\xi = 10$ (which means that ice is not very heterogeneous, for example, *Nechad et al.* (2005) used $\xi \approx 2$ for fiber matrix composite). Moreover, as $e_{01} = e_{02}$, ξ has just an influence on the parameter s^* , i.e. the critical stress above which damage starts.

The other parameters describing the deformation of the Eyring dashpot under an applied stress are β for the non-linear term and K for the linear one. It is difficult to infer such parameters for ice. *Nechad et al.* (2005) used for fiber matrix composite $\beta = 50 \cdot 10^{-9} \text{ Pa}^{-1}$ and $K = 10^5 \text{ s}^{-1}$. As ice is significantly weaker, we arbitrarily choose $\beta = 10^{-7} \text{ Pa}^{-1}$ and $K = 10^{-3} \text{ s}^{-1}$. With a tensile strength of ice equal to 1 MPa, we obtain from Eq. 3.5 $\frac{de}{dt} = 10^{-4} \text{ s}^{-1}$, which is coherent with the behavior of polycrystalline ice (*Schulson and Duval*, 2009).

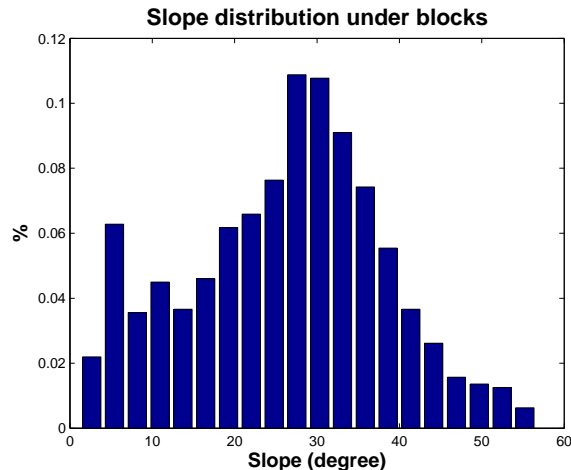


FIGURE 11. Distribution of the slope of the bedrock at the position of the blocks.

3.4. Geometric parameters. We have to consider the geometric input parameters for modeling Allalingsletscher. The glacier is discretized into a system of regular cubic blocks. As we saw in section 2.4, spatial extension of the glacier tongue evolved a lot during the last century. Digital elevation models (DEM) of the tongue for different years are available (see Fig. 5). In this study, we perform simulations for two extreme cases, one where the extension of the glacier tongue was maximum i.e. in 1982 and the other where the glacier broke-off i.e. in 2000. Since the glacier has completely retreated from the steep part, a detailed bedrock topography of the former glacier tongue could be obtained by a photogrammetric processing of recent aerial photographs (2008).

In order to obtain a realistic description of the damage and fragmentation process that may develop in the ice mass, we need a sufficiently large number of blocks.

As a compromise between reasonable sampling and numerical speed, we use a model composed of 20 m x 20 m blocks.

The spatial extensions of the glacier as well as the block heights in 1999 and 1982 is given by the respective DEM. The slope ϕ of the bedrock ranges from 0° to 45° (see Fig 11).

3.5. Extension of *Faillettaz et al. (2010)* model: accounting the effect of subglacial water flow. In our initial model, the effect of subglacial water flow on basal motion was not accounted. Basal processes play a key role in the instability (see 2.5). Melt water flow at the glacier bed influences the glacier dynamics (*Bell, 2008*) in two ways: (i) it lubricates the bed and (ii), if water becomes pressurized, the glacier can be partially decoupled from its bed. The lubrication of the bedrock leading to a progressive decrease of the ice-bedrock frictional resistance is modeled by decreasing the friction coefficient μ_0 (in Eq. 3.3) (*Faillettaz et al., 2011b*). The following assumptions are made:

- (1) The friction coefficient depends on the subglacial water pressure (*Schweizer and Iken, 1992; Jay-Allemand et al., 2011*).

- (2) The subglacial water pressure and discharge variations at the daily time scale are similar (*Boulton et al.*, 2007).
- (3) As a consequence of the two aforementioned assumptions, the decrease of the friction coefficient can be assumed to be proportional to the discharge of subglacial water flow.
- (4) The ice thickness does not vary drastically along the glacier tongue. Hence the gradient of the hydraulic potential and therefore the flow path of water is directly given by the topography of the bedrock (*Flowers and Clarke*, 1999).

At a first step, the amount of basal water flowing under each block has to be evaluate. We used a toolbox developed by *Schwanghart and Kuhn* (2010) to assess the subglacial drainage network with a DEM of the glacier bed. Most commonly DEMs are represented as rectangular grids where an elevation value is assigned to each cell. Two steps are needed to evaluate the basal water flow under each cell of the DEM. First, the flow direction is evaluated via a transfer matrix M . Elements in M contain the relative amount of discharge M_{ij} transferred from one cell i to a maximum number of eight downward neighbors with the index j . Thereby the transfer ratios are proportional to the downward slope to the respective neighbor. Second, by counting the number of cells draining in each grid cell, it calculates the upstream contributing drainage area. Finally, this toolbox gives the relative contribution from each cell of the DEM to the global runoff at the outlet. The amount of water flowing through a particular cell of the DEM is then obtained by multiplying the total runoff at the outlet by its relative contribution. Results are shown in Fig. 12.

In a second step, the friction coefficient is adapted according to the basal water discharge under each block with the following relationship:

$$(3.11) \quad \mu_o(i, j) = \mu_1 - Z_{ev}(i, j) \cdot Q \cdot c_p,$$

where μ_o is the friction coefficient of a given block (i, j) , μ_1 a constant friction coefficient, $Z_{ev}(i, j)$ is the relative contribution of the block, Q is the daily runoff at the glacier terminus and c_p is a parameter describing the relative influence of the basal water on the friction coefficient. In this way, the friction coefficient of a block is assumed to decrease when the local subglacial water discharge (and therefore the local subglacial water pressure) is increasing.

3.5.1. New algorithm accounting for subglacial basal water flow. The different steps describing how the instability is modeled are plotted in Fig. 13 and developed in Annexe 2. As explained previously, two phases have to be distinguished:

- (i) A quasi-static (quiescent) phase corresponding to the nucleation of block sliding and bond rupture.
- (ii) A dynamical (active) phase corresponding to the sliding phase of the blocks and the failure of bonds.

The new algorithm takes into account the subglacial water flow. At each time step of the run, the friction coefficient under each block is modified according to the local subglacial discharge. It is evaluated with Eq. 3.11 based on the runoff at the outlet given by the model of *Farinotti et al.* (2011) and the matrix Z_{ev} calculated from the DEM of the bedrock topography.

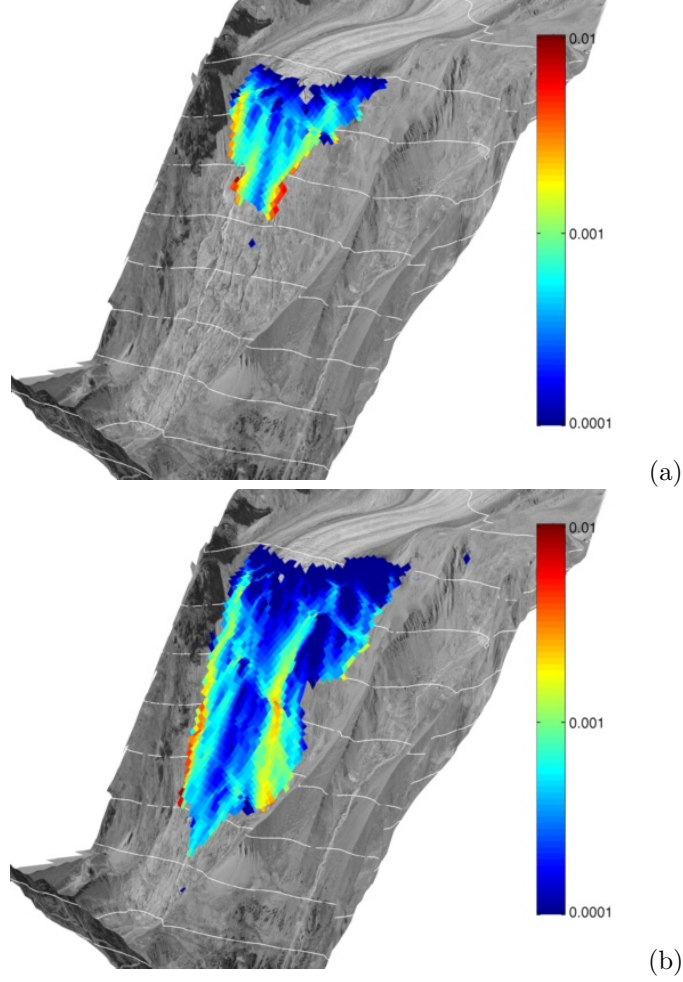


FIGURE 12. Relative contribution of each block to the total subglacial water discharge (Z_{ev}) for 1999 (a) and 1982 (b). Red zones indicate where discharge of subglacial water is large.

4. NUMERICAL RESULTS

The aim of the numerical simulations is to better understand the development of a glacier sliding instability, considering Allalingletscher as an example. In particular, we intend to provide answers to the following questions:

- Why did the glacier only broke off in 1965 and 2000?
- Does the glacier geometry play a role in the occurrence of the break-off?
- What is the influence of subglacial water on the glacier dynamic and on the break-off?
- Does the subglacial drainage network efficiency play a role in the onset of the instability?
- Is it possible to find precursory signs of the break-off?
- Would it be possible to predict the break-off?

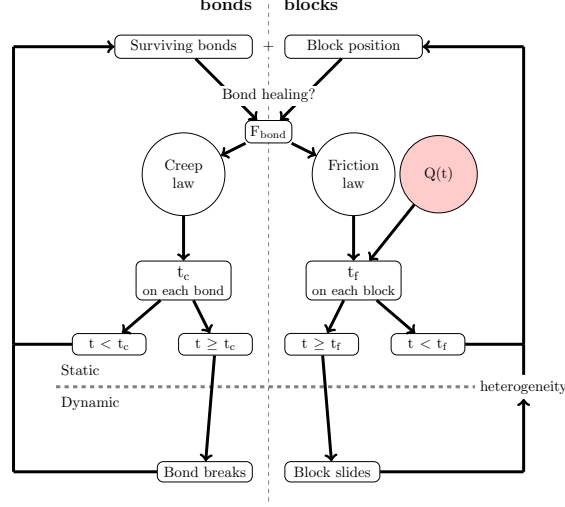


FIGURE 13. Schematic flowchart of this **modified spring-block** model accounting for subglacial water flow.

4.1. Tuning the creep parameters. The first step of the numerical simulation is to find plausible creep parameters able to reproduce the observed glacier behavior. Creep parameters turn out to be crucial. As explained in section 3.3, the creep parameters are β and C . *Faillettaz et al.* (2010) showed that three different regimes can be expected from the model, namely a fragmentation regime, slab regime or stick and slip regime. As showed in section 2.4, the glacier broke off in 2000 as a slab avalanche. So we have to find a parameter set able to reproduce the observed behavior.

In this part, we will use the 1999 surface topography for our simulation. At each time step, we evaluate, for each block, the basal slope (see Fig. 2). We performed different runs with the 1999 glacier geometry by varying creep parameters. Results are shown in Fig. 14.

In the fragmentation regime, creep occurs before the nucleation of sliding could develop, so that bonds break and the bottom part undergoes a fragmentation process with the creation of a heterogeneous number of sliding blocks (Fig. 14(b)). In the stick-slip regime, the time needed for damage initiation is so great that the whole glacier tongue undergoes a series of internal stick slip events, associated with an initial slow average downward motion. After a sufficient time, all blocks slide (Fig. 14(d)). In the slab regime, in which neither damage nor frictional sliding dominates, the occurrence of a macrocrack propagating roughly along the location of the largest curvature associated with the change of slope from the stable frictional regime in the upper part to the unstable frictional state in the lower part (Fig. 14(c)).

In the following, we used the parameter set that reproduces the last regime.

4.2. Influence of the glacier geometry on the instability. To investigate the contribution of the glacier geometry on the onset of the instability, we performed

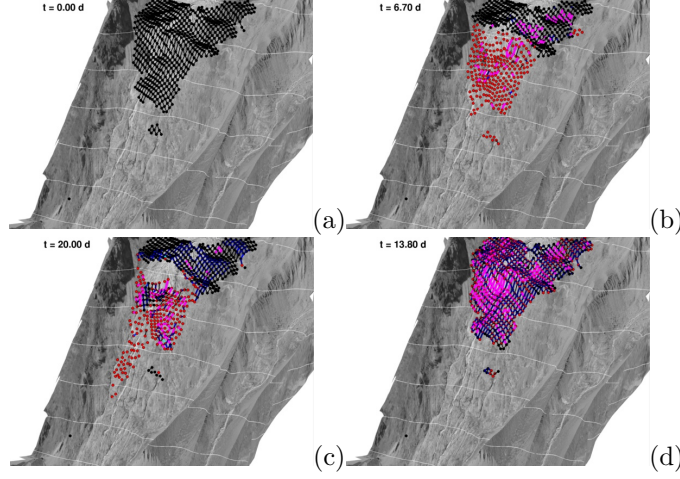


FIGURE 14. Snapshots illustrating the three possible regimes: fragmentation (b), slab (c) and stick-slip(d)

TABLE 1. Numerical values of parameters used in our simulations.

Friction parameters					
A	θ_0	μ_0	δ_0		
-	d	-	$m.d^{-1}$		
0.1	100	0.8	10^{-3}		
Creep parameters					
E	β	$C \sim 1/K$	ξ	e_{01}	e_{02}
Pa	Pa^{-1}	s	-	-	-
10^9	10^{-7}	10^3	10	0.003	0.003
Runoff parameters					
μ_1	c_p				
0.8	6				

numerical simulation on two different glacier geometries in year 2000 (when a break-off occurred) and year 1982 (when active phase could be evidenced without break-off). We initialized our simulation as described in the previous section. Table 1 summarizes the parameters used in our simulations.

Fig. 15 shows the results of simulations for both geometries of 2000 and 1982 with the same creep and friction parameters. As the terminal part of the glacier lies on a average slope of 30° , we imposed the friction coefficient to be a bit lower than its mean slope, i.e. $\mu_0 = 0.5$.

With this set of parameters, the initiation of the instability could be reproduced. At the beginning of both simulations, blocks situated in the steepest part start to slide, inducing a zone with high tension at the slope changes. Then, blocks located downstream start to slide resulting in the apparition of a compression zone directly downstream of this process zone (Fig. 15(b)). This compression zone grows as the instability develops. In the case of the 1982 geometry, the compression zone

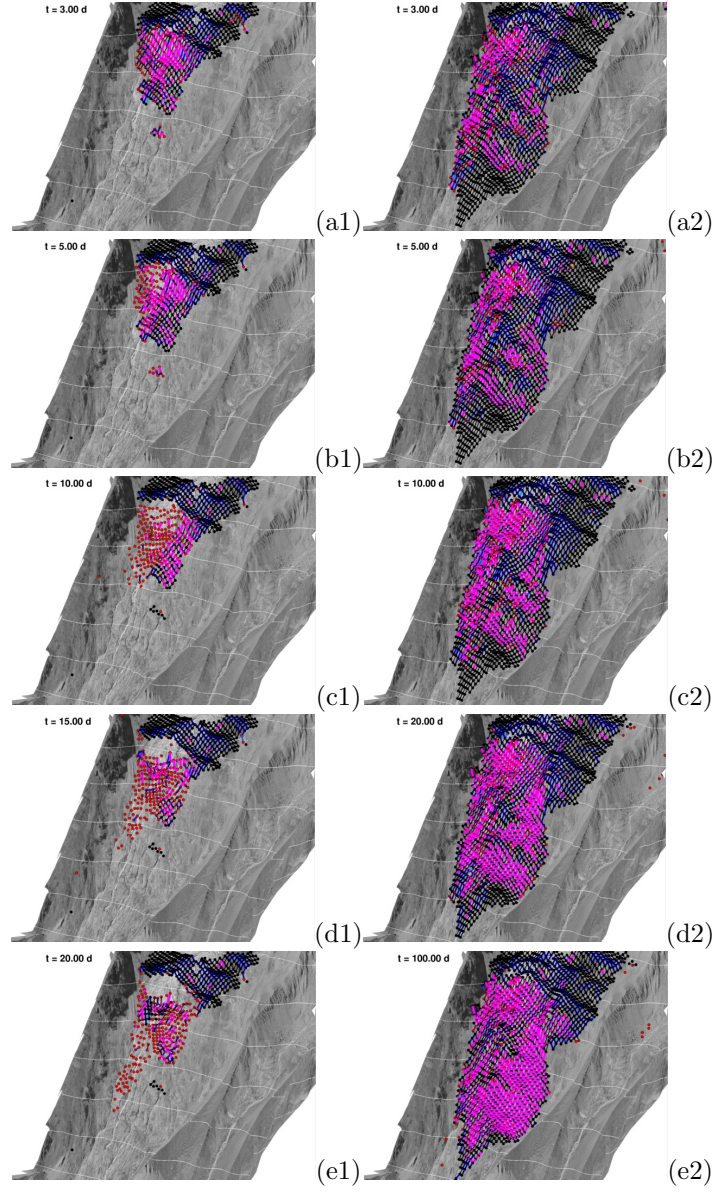


FIGURE 15. Snapshot describing the rupture progression for the glacier geometry in the years 2000 and 1982, with a constant friction coefficient.

continues to propagate downwards and reaches the terminus where the glacier is less steep. The whole glacier is then supported by the lower part of the tongue, which stabilizes the glacier and stops the development of the instability (Fig. 15(e2)). On the contrary, in the case of the 2000 geometry, the compression zone reaches the terminus where the slope is still large. Nothing supports the advance of the glacier, resulting in a global break-off of the tongue (Fig. 15(e1)).

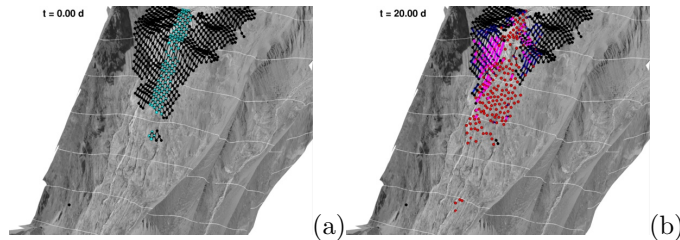


FIGURE 16. (a) Blue blocks indicate where friction coefficient was changed. (b) Snapshot at the end of the run.

The geometrical configuration of the glacier tongue plays therefore a major role in the development of the instability. In the case of Allalingletscher, the glacier tongue where the terminus is located beyond the position of 1965 is stabilized as the slope near the terminus is lower.

4.3. Role of subglacial water: Channelized vs. distributed subglacial drainage network.

4.3.1. Channelized subglacial drainage network. We pointed out that the subglacial water and drainage network play a role in the initiation and the development of the instability. The presence of subglacial water could be modeled by decreasing the friction coefficient as a function of discharge (see 3.5).

To investigate the relative contribution of the drainage network at the onset of the instability, we performed different type of simulations. We have already shown in section 4.1 that a global decrease of the friction (i.e. modeling a distributed subglacial drainage network) could qualitatively reproduce the break-off event in the year 2000.

To study the effect of a channelized drainage network, we performed a simulation where the friction coefficient was decreased locally, in a band roughly situated at the center of the glacier (Fig 16a). The band width was set to 3 blocks, i.e. 60 m. This allows to reproduce the effect of a flow path of subglacial water in a restricted area. Results are shown in Fig. 16. After the development of the crown crevasse, the instability develops, leading to a localized break-off with a triangular shape. Moreover, to obtain such a rupture, the friction coefficient had to be set to a very low value ($\mu_0 = 0.2$), indicating a stronger stability in the case of a channelized network than with a distributed one. A channelized network could not reproduce, even qualitatively, the break-off event of the year 2000.

4.3.2. Distributed subglacial drainage network. We performed two runs with the same creep and friction parameters but for two different years (1982 and 2000). For these 2 years, modeled daily runoff at the outlet of the glacier are available (red lines in Fig. 17). The model allows to redistribute the water under each block according to Eq. 3.11 (Fig. 12).

Fig. 18 shows the evolution of the instability for the years 2000 and 1982. In 2000, after the opening of the crown crevasse and the formation of a compressive zone at the glacier tongue (Fig. 17(a)), the glacier enters in a quiescent regime. Even the increase in runoff in May does not affect the dynamic of the glacier tongue (Fig. 17(a)). Suddenly, after 165 days of simulation (in mid-June), the

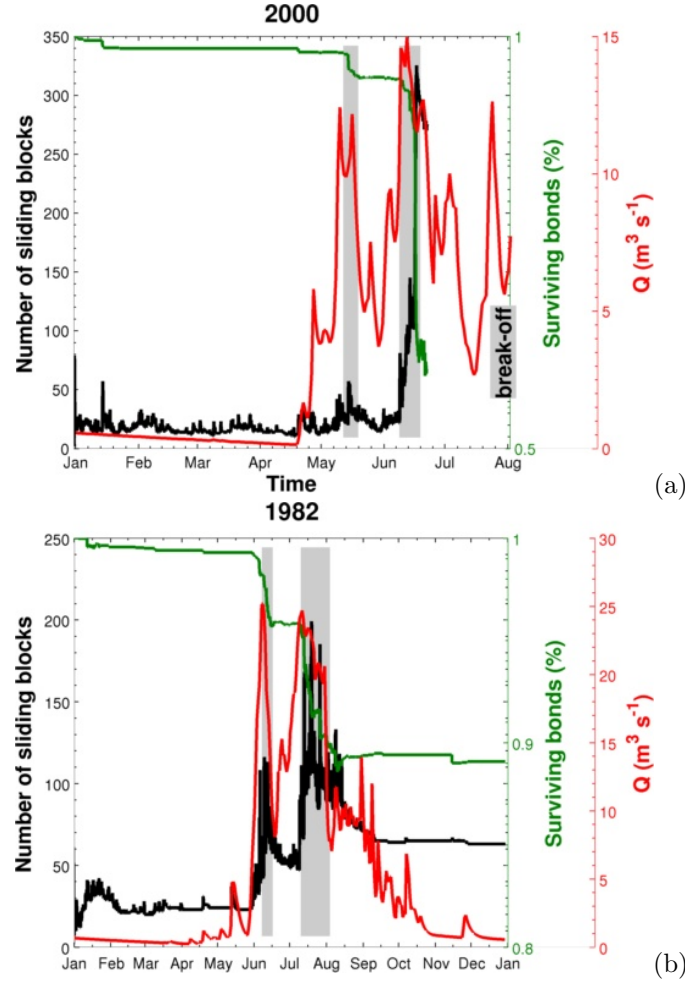


FIGURE 17. Runoff, number of sliding blocks and surviving bonds as a function of time for the situation in 2000 (a) and 1982 (b)

tongue starts to be unstable, resulting in a fragmentation process that propagates over the whole tongue in a few days. We stopped the simulation when the glacier tongue was completely disaggregate. In 1982, the situation is different as the tongue extension is larger. The compression zone propagates downstream until the lowest glacier tongue, where the bed slope decreases. An increase in the number of sliding blocks can be noticed between mid July and beginning of September (Fig. 17(b)), indicating an ongoing active phase. Interestingly, this active phase is not directly correlated with the runoff magnitude, as it drops in August in the course of the ongoing active phase. It also appears that once triggered, the active phase needs some time to stop.

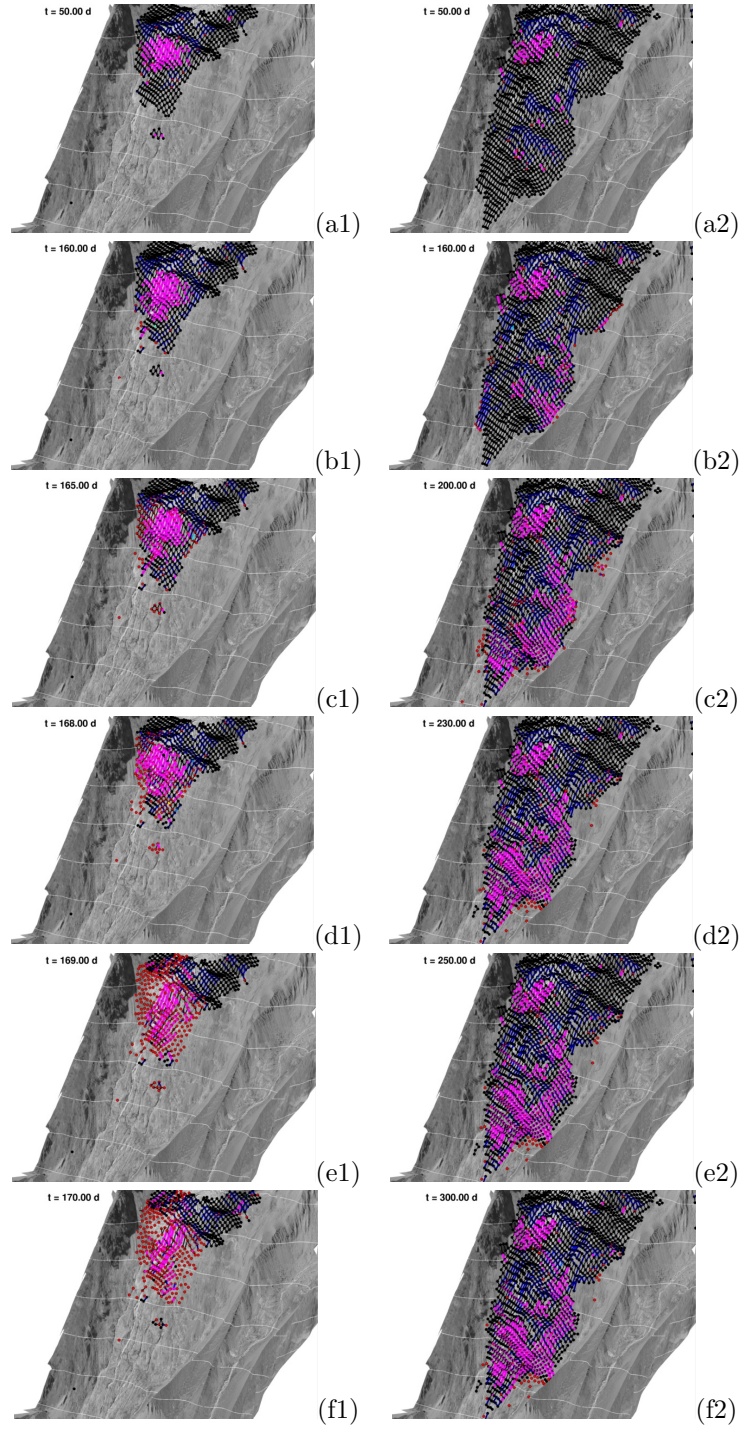


FIGURE 18. Snapshots describing the rupture progression and sliding instability in the block lattice for the years 2000 and 1982.

5. DISCUSSION

With the results obtained with our model, we could highlight the mechanisms leading to the sliding instability. The main result is that the active phase is triggered by an increase of subglacial water flow, its duration depending on the extension of the glacier tongue.

5.1. Existence of active phases and prediction. An ongoing active phase does not necessarily lead to a catastrophic break-off. Some further conditions are required to trigger the large scale rupture:

- (i) A critical geometric configuration of the glacier tongue,
- (ii) A distributed drainage network.

This explains why such instabilities are so rare.

Our model is able to explain and predict the occurrence of the active phases observed on Allalingsletscher, but not the final catastrophic break-off. For the situation in year 2000, the model could reproduce with a good timing the active phase appearing before the final rupture. In the following, as the glacier is completely disaggregated, the simulation could not be pursued and the occurrence of the break-off event could not be predicted. Moreover, the rapid motion of the disaggregated glacier likely affected the efficiency of the subglacial drainage network. This process could lead to a positive feedback: an enhanced basal motion affects the efficiency of subglacial drainage network leading to increase subglacial water pressure and basal motion further. This positive feedback induced by the onset of the active phase is not modeled.

5.2. Impact of the runoff evolution on the break-off. Our results show for both years 2000 and 1982 that fragmentation phases (drop of surviving bonds highlighted by gray bands in Fig. 17) coincide with periods where the daily runoff is decreasing. On the contrary, when the runoff increases, the bond breaking process is suddenly stopped. Moreover, the glacier motion reacts to runoff variations with a delay depending on its size. Fig. 17 indicates a clear correlation between runoff magnitude and the number of sliding blocks with a larger delay in 1982 than 2000.

These results provide new insights on the maturation process of the instability. They suggest the following sequence of ongoing processes:

- (1) The onset of the active phases is induced by an increase of subglacial water flow with a delay depending on its size.
- (2) The initiation of the fracturation process starts in a period of decreasing runoff, i.e. during a rapid recoupling phase of the glacier onto its bedrock. During this phase, an intensive fracturation of the glacier tongue is initiated.
- (3) A catastrophic break-off requires the combination of two opposite phenomena: first, the glacier needs to be in an active phase with a strong enhanced basal motion, and second, this active phase must be stopped abruptly with a rapid recoupling of the glacier to its bed.

The likelihood of this process chain can be verified with observations during the years 2000 (Fig. 17(a)) and 1965 (Fig. 19) when the glacier broke off. It appears that, for both years, one month before the rupture, the runoff drastically increases, which could lead to an active phase. During the 6 days prior to the break-off, the runoff dropped from 13 to 5 m³ s⁻¹ in 2000 and from 14 to 5 m³ s⁻¹ in 1965.

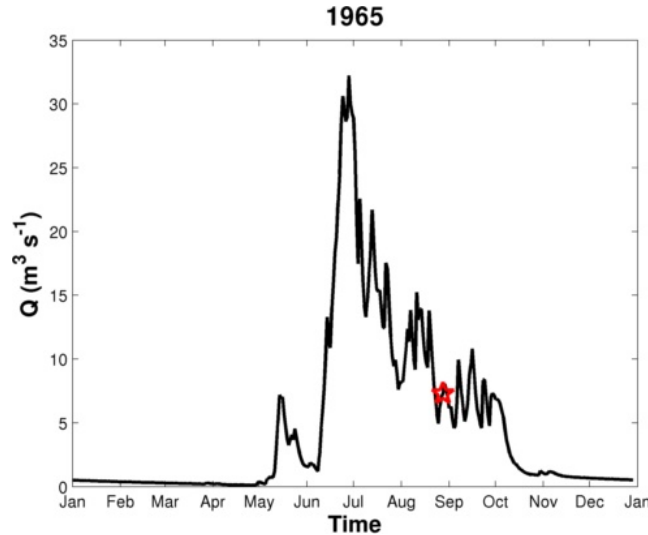


FIGURE 19. Modeled runoff regime in the year 1965 (The red star represents the break-off).

It appears that the process chain leading to the final break-off in 1965 and 2000 inferred by our modeling results is confirmed by these observations.

With these new insights explaining the sliding instabilities for Allalingletscher, we can analyse other situations.

5.3. Analysis of observed sliding instabilities of other glaciers.

5.3.1. Break-off of Le glacier du Tour (France). The terminal tongue of the glacier du Tour (Mont Blanc, France) broke off on August 14th 1949. The estimation of the volume of the break-off ranges from 0.5 to 2 millions cubic meters (Glaister, 1951). At that time, the glacier geometry was similar to Allalingletscher. The upper part of the glacier was lying on a flat zone, whereas its tongue ended in a very steep terrain (about 40 degrees) that is not able to support the glacier tongue. The geometrical configuration of the glacier tongue was also in a critical configuration. Moreover, different subglacial streams emerging from the glacier could be distinguished, indicating a distributed subglacial drainage network (see Fig. 20). The two main criteria for a break-off in the case of a sliding instability were likely met. Meteorological conditions prevailing in this area were analyzed (Fig. 21) to infer a runoff history prior to the break-off event. This temperature time series indicates that in the month preceding the break-off, temperatures were high (about 10 °C at 2472 m). Five days before the break-off, the temperatures dropped from 14 to 0 °C. Subglacial runoff magnitude should have drastically decreased during this period. This confirms that the recoupling of the glacier on its bed played a decisive role in the break-off event.

5.3.2. Triftgletscher (Bernese Alps, Switzerland). The Triftgletscher is situated in the Bernese Alps in Switzerland. The glacier experienced a rapid retreat during the last 20 years. After the year 2000, the tongue ended in a steep terrain (about 35 degree) and its stability was questionable (Dalban *et al.*, 2011). In the following

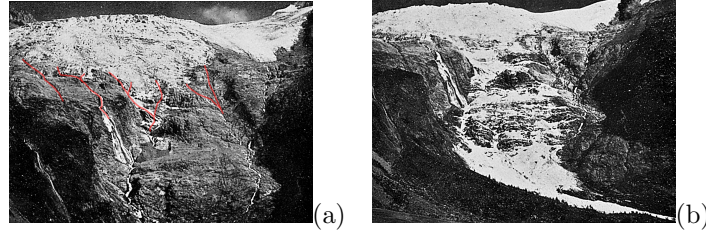


FIGURE 20. Le glacier du Tour in 1949 (a) before the break-off (the possible drainage network highlighted in red (b) after the break-off

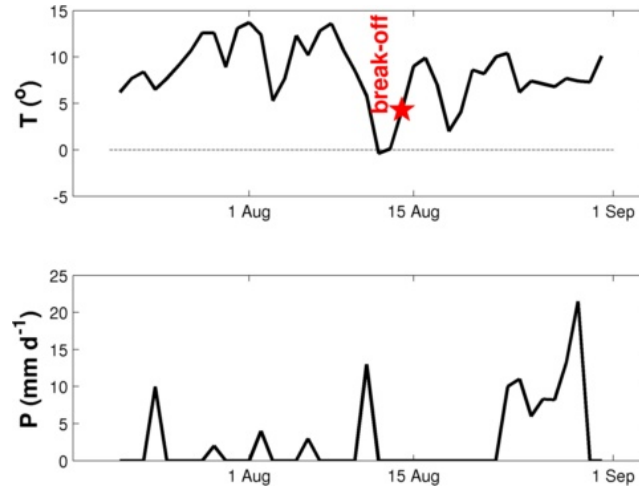


FIGURE 21. Temperature and precipitation in summer 1949 at the Col du Grand Saint Bernard (2472 m a.s.l.), located about 20 km South West from the Glacier du Tour. The break-off is indicated with a red star.

summer surface velocities increase from 1 to 4 m d^{-1} , similar to a mini-active phase. However, up to now, the glacier did not break-off.

All the basic conditions for the glacier to break-off were fulfilled, except the existence of a distributed subglacial drainage network. This might be the reason for the absence of the initiation of active phase here.

5.3.3. Giesengletcher (Bernese Alps, Switzerland). In a more general context, climate change may affect the stability of sliding glaciers. As a general glacier retreat in the Alps is observed, the geometry of some glaciers might potentially evolve toward a critical situation. As an example, Giesengletscher (Bernese Alps, Switzerland) would be a suitable candidate to a future catastrophic break-off. The terminus of Giesengletscher is located at about 2500 m a.s.l. in the Bernese Alps (Fig. 22). In 2008, a crevasse spanning the whole glacier was observed on the glacier tongue indicating an ongoing active phase on the steepest part (about 35 degree, Fig. 22(a)). The situation is nevertheless not critical yet, as the glacier terminus is resting on a moderate slope, which stabilizes the glacier tongue (green zone in Fig.

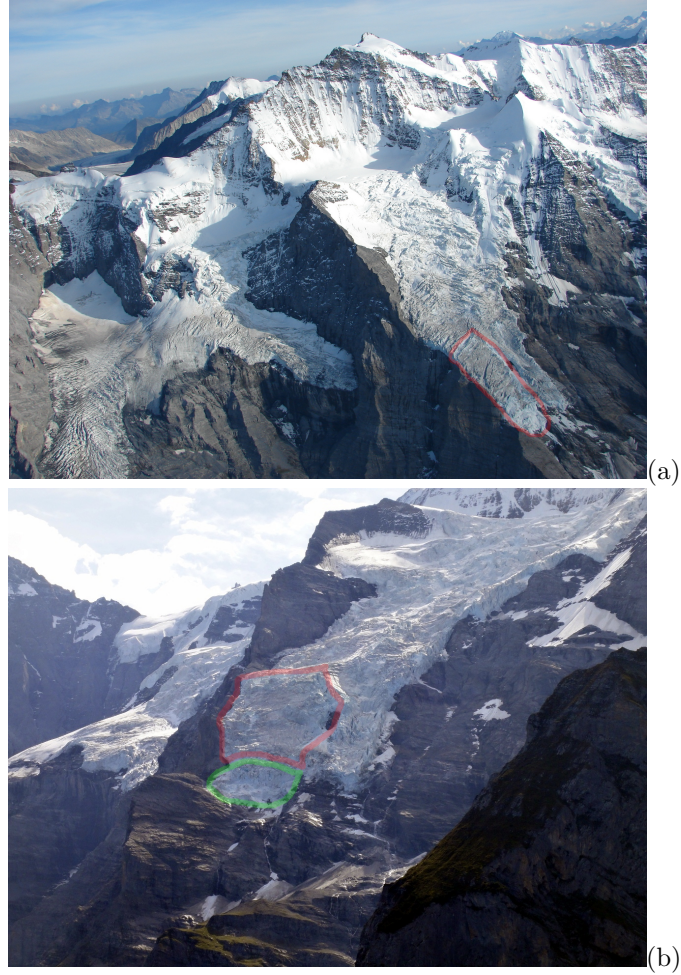


FIGURE 22. (a) Situation of Giesengletscher in 2008 (highlighted in red). (b) Situation in 2011. Green zone indicates the stable part of the tongue, in red the possible unstable zone.

22(b)). Moreover, its bedrock is likely smooth, so that the drainage network is expected to be distributed. Except for the geometrical configuration of the tongue, all conditions for the glacier to break-off are fulfilled, indicating that the disappearance of the supporting glacier terminus could lead to a critical situation, as the tongue geometry would become critical.

6. CONCLUSIONS

Glacier sliding instabilities may occur on temperate glacier tongues. Such instabilities are strongly affected by the subglacial hydrology: infiltrated melt water may indeed cause (i) a lubrication of the bed and (ii) a decrease of the effective pressure at the glacier bed and consequently a decrease of basal friction. Available data from Allalingsletscher (Valais, Switzerland) indicate that the glacier tongue

experienced an active phase during 2-3 weeks in summer in most years between 1965-2000 with strongly enhanced basal motion. This glacier broke-off twice in 1965 and 2000. In order to scrutinize in more detail the processes governing the sliding instabilities, a numerical model developed to investigate gravitational instabilities in heterogeneous media was applied to Allalingsletscher. This modified spring-block model enables to account for various geometrical configurations of the glacier and also for interactions between basal sliding and tension cracking. The impact of subglacial water flow on basal motion was included in the model.

Our results indicate that basically three conditions have to be fulfilled for a break-off to occur in the case of a sliding instability: (i) a critical geometrical configuration of the glacier tongue is needed, where the glacier terminus rests on a steep slope. (ii) the glacier has to experience an “active phase” during which basal motion drastically increases, (iii) the subglacial drainage network has to be distributed. Moreover, our modeling results point out that the break-off always occurs after a sudden phase of recoupling of the glacier on its bedrock, characterized by a drop of subglacial water flow. This new precursory sign was observed for both 1965 and 2000 break-off event. We also showed that all these conditions were fulfilled in 1949 before the break-off of the glacier du Tour, and moreover, we demonstrated that the same drop of subglacial water runoff occurred five days before the catastrophic break-off, indicating that this new precursory sign might be decisive. In a more general context, climate change may affect the stability of steep glacier tongues, as they retreat and may evolve toward a critical geometry. This model casts a gleam of hope for a better understanding of the ultimate rupture of such glacier sliding instabilities.

INITIATION OF SLIDING FOR A SINGLE BLOCK

This appendix complements Section 3.2 by providing details of the calculation of the critical time at which unstable sliding of a given block occurs. Section 3.2 describes the sub-critical sliding process of a given block interacting via state-and-velocity solid friction with its inclined basal surface. When the sub-critical sliding velocity $d\delta/dt$ diverges (we refer to the time when this occurs as the “critical time” t_f for the frictional sliding instability), this indicates a change towards a dynamical sliding regime where inertia (the block mass and its acceleration in the Newton’s law) has to be taken into account.

Let us calculate explicitly how the critical time t_f is obtained and define its dependence on the parameters and boundary conditions. Let us call $T \equiv \|\sum \vec{F}_{\text{bond}} - T_{\text{weight}}\vec{x}\|$ (or $N \equiv N_{\text{weight}}$) the total shear (or normal) force exerted on a given block, where \vec{F}_{bond} is the force exerted by a neighboring spring bond, and N_{weight} and T_{weight} are the normal and tangential forces due to the weight of the block. We then have

$$(1) \quad \mu = \frac{T}{N} = \tan \phi ,$$

where ϕ is the angle of the basal surface supporting the block. Therefore,

$$(2) \quad \mu_0 + A \ln \frac{\dot{\delta}}{\dot{\delta}_0} + B \ln \frac{\theta}{\theta_0} = \tan \phi .$$

As explained in Section 3.2, $A - B$ is usually very small for natural material, of the order of $A - B \approx \pm 0.02$. For the sake of simplicity, we assume $A = B$. As recalled

in Section 3.2, this choice is not restrictive as it recovers the two important regimes (*Helmstetter et al.*, 2004). This leads to

$$(3) \quad \ln \frac{\dot{\delta}}{\dot{\delta}_0} \frac{\theta}{\theta_0} = \frac{\tan \phi - \mu_0}{A} ,$$

whose solution is

$$(4) \quad \dot{\delta} \theta = (\dot{\delta}_0 \theta_0) \exp \left(\frac{\tan \phi - \mu_0}{A} \right) .$$

Combining Eqs. 3.2 and .4, we obtain

$$(5) \quad \dot{\theta} = 1 - \frac{\theta \dot{\delta}}{D_c} = 1 - \frac{\dot{\delta}_0 \theta_0}{D_c} \exp \left(\frac{\tan \phi - \mu_0}{A} \right) .$$

After integration it reads

$$(6) \quad \theta = \theta_0 + \left(1 - \frac{(\dot{\delta}_0 \theta_0) \exp \left(\frac{\tan \phi - \mu_0}{A} \right)}{D_c} \right) t ,$$

and using Equation (.4), we obtain

$$(7) \quad \dot{\delta} = \frac{(\dot{\delta}_0 \theta_0) \exp \left(\frac{\tan \phi - \mu_0}{A} \right)}{\theta_0 + \left(1 - \frac{\dot{\delta}_0 \theta_0}{D_c} \exp \left(\frac{\tan \phi - \mu_0}{A} \right) \right) t} .$$

This expression exhibits the usual regimes: a finite time singularity is obtained for $(\dot{\delta}_0 \theta_0) \exp \left(\frac{\tan \phi - \mu_0}{A} \right) > D_c$. In this case, Expression (.7) can be re-written as

$$(8) \quad \dot{\delta} = \frac{D_c \dot{\delta}_0 \theta_0 \exp \left(\frac{\tan \phi - \mu_0}{A} \right)}{D_c - \dot{\delta}_0 \theta_0 \exp \left(\frac{\tan \phi - \mu_0}{A} \right)} \cdot \frac{1}{t_f - t}$$

with

$$(9) \quad t_f = \frac{D_c \theta_0}{D_c - \dot{\delta}_0 \theta_0 \exp \left(\frac{\tan \phi - \mu_0}{A} \right)} .$$

We can simplify Expression (.8) by using the condition that, for $\mu = \tan \phi = \mu_0$, we should have $t_f \rightarrow \infty$. But, for $\mu = \mu_0$, $\exp \left(\frac{\mu_s - \mu_0}{A} \right) = 1$ and thus, for the condition $t_f \rightarrow \infty$ to hold, we need

$$(10) \quad \frac{\dot{\delta}_0 \theta_0}{D_c} = 1 .$$

The final expression for the critical time t_f signaling the transition from a subcritical sliding to the dynamical inertial sliding is, for $\mu > \mu_0$,

$$(11) \quad t_f = \frac{\theta_0}{\exp \left(\frac{\mu_s - \mu_0}{A} \right) - 1} ,$$

while $t_f \rightarrow \infty$ for $\mu \leq \mu_0$. Note that the dependence on $\dot{\delta}_0$ has disappeared due to the relation (.10).

To summarize, a given configuration of blocks and spring tensions determines the value of $T \equiv \left\| \sum \vec{F}_{\text{bond}} - T_{\text{weight}} \vec{x} \right\|$ and $N \equiv N_{\text{weight}}$ and therefore of μ via (.1). Knowing μ and given the other material parameters θ_0, μ_0 and A , we determine

the time t_f for the transition to the dynamical regime for that block via Equation (.11).

GENERAL ALGORITHM

The simulation of the frictional process for each given block proceeds as follows:

- (1) A given configuration of blocks and spring tensions determines the value of $T \equiv \|\sum \vec{F}_{\text{bond}} - T_{\text{weight}}\vec{x}\|$ and $N \equiv N_{\text{weight}}$ for each block, and therefore their solid friction coefficient μ corresponds to the ratio T/N .
- (2) At a given time, knowing the runoff at the outlet, μ_0 is evaluated for a given block with Eq. 3.11.
- (3) Knowing μ for a given block and with the other material parameters θ_0, μ_0 and A for that block, the time t_f for the transition to the dynamical sliding regime is calculated with expression (3.3). Eq. 3.3 for t_f gives the waiting time until the next block starts to slide.
- (4) When the block undergoes a transition into the dynamical sliding regime at time t_f , its subsequent dynamics should obey Newton's law.
- (5) The dynamical slide of the block goes on as long as the velocity of the block remains positive. When its velocity reaches zero, we assume that the block is no more sliding. To account for the heterogeneity and roughness of the sliding surface, we assume that the state variable θ_0 is reset to a new random value after the dynamical sliding stops. This random value is taken to reflect the characteristics of the new asperities constituting the fresh surface of contact.
- (6) After a dynamical slide, the forces exerted by the springs that connect the block to its neighbors are updated, as is the new gravitational force (if the basal surface has a curvature), the new value of μ is obtained, the time counter for frictional creep is reset to zero, and a new process of slow frictional creep develops over the new waiting time t_f , that is, in general, different from the previous one.

In summary, simulation of the damage process leading to bond rupture between blocks proceeds as follows.

- (1) Given an initial configuration of all the blocks within the network, the elastic forces exerted by all bonds can be calculated from their extension/compression.
- (2) For each bond i subjected to an initial stress $s_0(i)$, we calculate the corresponding critical time $t_{c,0}(i)$ at which it would rupture if neither of the two blocks connected to it moved in the meantime. For those bonds where $s_0(i) < s^*$ defined in Equation (3.8), $t_{c,0}(i)$ is infinite.
- (3) Some bonds will eventually fail, modifying the force balance on their blocks and accelerating the transition to the sliding regime, after which the stresses in the bonds connected to the same blocks are modified.

REFERENCES

- Andersen, J.V., D. Sornette and K.-T. Leung (1997), Tri-critical behavior in rupture induced by disorder, *Phys. Rev. Lett.*, **78**, 2140-2143.
- Barnes, P., D. Tabor, F. R. S. Walker and J. C. F. Walker (1971), The friction and creep of polycrystalline ice. *Proc. Roy. Soc. Lond. A.*, **324**, 127-155.

- Bell, R.E. (2008). The role of subglacial water in ice-sheet mass balance. *Nature Geosci.*, 1(5), 297-304.
- Boulton, G.S., R. Lunn, P. Vidstrand, S. Zatsepin (2007), Subglacial drainage by groundwater-channel coupling, and the origin of esker systems: Part 1-glaciological observations, *Quaternary Sci. Rev.*, 26, (7-8), 1067-1090, 10.1016/j.quascirev.2007.01.007.
- Dalban-Canassy, P., A. Bauder, M. Dost, R. Fähr, M. Funk, S. Margreth, B. Müller and S. Sugiyama (2011), Hazard assessment investigations due to the recent changes in Triftgletscher. *Nat. Hazard Earth Sys.*, 11:2149-2162.
- Dieterich, J.H. (1994), A constitutive law for rate of earthquake production and its application to earthquake clustering, *J. Geophys. Res.*, 99, 2601-2618.
- Faillietaz, J., A. Pralong, M. Funk and N. Deichmann (2008), Evidence of log-periodic oscillations and increasing icequake activity during the breaking-off of large ice masses. *J. Glaciol.*, 57, (187), 725.
- Faillietaz, J., D. Sornette, and M. Funk (2010), Gravity-driven instabilities: interplay between state-and-velocity dependent frictional sliding and stress corrosion damage cracking. *J. Geophys. Res.*, 115, B03409, doi:10.1029/2009JB006512. arXiv/0904.0944.
- Faillietaz, J., M. Funk and D. Sornette (2011a), Icequakes coupled with surface displacements for predicting glacier break-off. *J. Glaciol.*, 57, 203, 453-460. arXiv:1011.4781v1
- Faillietaz, J., D. Sornette and M. Funk (2011b), Numerical modeling of a gravity-driven instability of a cold hanging glacier: reanalysis of the 1895 break-off of Altelsgletscher, Switzerland. *J. Glaciol.*, 57, 205, 817-831.
- Farinotti, D., S. Usselmann, M. Huss, A. Bauder and M. Funk (2011), Runoff evolution in the Swiss Alps: Projections for selected high-alpine catchments based on ENSEMBLES scenarios. *Hydrol. Process.*, Accepted, doi: 10.1002/hyp.8276.
- Flowers, G. E. and G. K. C. Clarke (1999), Surface and bed topography of Trapidge Glacier, Yukon Territory, Canada: digital elevation models and derived hydraulic geometry. *J. Glaciol.*, 45 (149), 165-174.
- Fortt, A.L. and E.M. Schulson (2009), Velocity-dependent friction on Coulombic shear faults in ice. *Acta Mater.*, 57, 4382-4390.
- Glaciological reports (1881-2009), The Swiss Glaciers, 1880- 2004/05, 1-126, Yearbooks of the Cryospheric Commission of the Swiss Academy of Sciences (SC-NAT), published since 1964 by Laboratory of Hydraulics, Hydrology and Glaciology (VAW) of ETH Zürich.
- Glaister R.M (1951), The ice slide on the Glacier du Tour *J. Glaciol.*, 1, (9), 508-509.
- Helmstetter, A., D. Sornette, J.-R. Grasso, J. V. Andersen, S. Gluzman and V. Pisarenko. 2004. Slider-Block Friction Model for Landslides: Application to Vaiont and La Clapiere Landslides, *J. Geophys. Res.*, 109, B02409, doi:10.1029/2002JB002160.
- Huss, M., R. Hock, A. Bauder and M. Funk (2010), 100-year mass changes in the Swiss Alps linked to the Atlantic Multidecadal Oscillation. *Geophys. Res. Lett.*, 37, L10501, doi:10.1029/2010GL042616.
- Hutter, K. (1983), Theoretical glaciology; material science of ice and the mechanics of glaciers and ice sheets. D. Reidel Publishing Company/Tokyo, Terra Scientific Publishing Company.

- Jay-Allemand, M., F. Gillet-Chaulet, O. Gagliardini and M. Nodet (2011), Investigating changes in basal conditions of Variegated Glacier prior to and during its 1982-1983 surge, *The Cryosphere*, 5, 659-672, doi:10.5194/tc-5-659-2011.
- Kennedy, F.E., E.M. Schulson and D.E. Jones (2000), The friction of ice at low sliding velocities, *Philos. Mag. A*, 80 (5) 1093-1110.
- Leung, K. and J.V. Andersen (1997), Phase transition in a spring-block model of surface fracture, *Europhys. Lett.*, 38 (8), 589-594.
- Lishman, B., P. Sammonds and D. Feltham (2011), A rate and state friction law for saline ice. *J. Geophys. Res.*, in press. doi:10.1029/2010JC006334.
- Maeno, N. and M. Arakawa. (2004), Adhesion shear theory of ice friction at low sliding velocities, combined with ice sintering. *J. Appl. Phys.*, 95(1), 134-139.
- Mikumo, T., K. B. Olsen, E. Fukuyama and Y. Yagi (2003), Stress-breakdown time and slip-weakening distance inferred from slip-velocity functions on earthquake faults, *Bull. Seism. Soc. Am.*, 93, 264-282.
- Montagnat, M. and E. Schulson (2003), On friction and surface cracking during sliding of ice on ice. *J. Glaciol.*, 49 (166), 391-396.
- Nechad, H., A. Helmstetter, R. El Guerjouma and D. Sornette (2005), Creep Ruptures in Heterogeneous Materials, *Phys. Rev. Lett.*, 94, 045501.
- Ohmura, A. and H. Kawamura (2007), Rate- and state-dependent friction law and statistical properties of earthquakes. *Europhys. Lett.*, 77, (6), 69001 (5pp).
- Petrovic, J.J. (2003), Mechanical properties of ice and snow. *J. Mater. Sci.*, 38, 1-6.
- Petrenko, V.F. and R.W. Whitworth (1999), Physics of ice. Oxford University Press, 384pp.
- Pralong, A. and M. Funk (2006), On the instability of avalanching glaciers, *J. Glaciol.*, 52 (176): 31-48.
- Röthlisberger, H. and P. Kasser (1978), The readvance of the Allalingsletscher after the ice avalanche of 1965. *Materialy Glyatsiologicheskikh Issledovaniy. Khronika Obsuzhdeniya*, 33, 152-164.
- Scholz, C.H. (1998), Earthquakes and friction laws, *Nature*, 391, 37-42.
- Scholz, C.H. (2002), The mechanics of earthquakes and faulting (Cambridge University Press).
- Schwanghart, W. and N.J. Kuhn (2010) TopoToolbox: A set of Matlab functions for topographic analysis. *Environ. Modell. Softw.*, 25, 770-781.
- Schweizer, J. and A. Iken (1992) The role of bed separation and friction in sliding over an undeformable bed. *J. Glaciol.*, 38 (128), 77-92.
- Schulson, E.M. and P. Duval (2009), Creep and fracture of ice (Cambridge University Press).
- Vaughan, D. (1995), Tidal flexure at ice shelf margins. *J. Geophys. Res.*, 100 (B4), 6213-6224.
- Zhang, W., T. Iwata, K. Irikura, H. Sekiguchi and M. Bouchon (2003), Heterogeneous distribution of the dynamic source parameters of the 1999 Chi-Chi, Taiwan, earthquake, *J. Geophys. Res.*, 108 (B5), 2232, doi:10.1029/2002JB001889.

LABORATORY OF HYDRAULICS, HYDROLOGY AND GLACIOLOGY (VAW), ETH ZURICH, CH-8092 ZÜRICH, SWITZERLAND.

E-mail address: `faillettaz@vaw.baug.ethz.ch`

LABORATORY OF HYDRAULICS, HYDROLOGY AND GLACIOLOGY (VAW), ETH ZURICH, CH-8092 ZÜRICH, SWITZERLAND.

DEPARTMENT OF MANAGEMENT, TECHNOLOGY AND ECONOMICS, ETH ZÜRICH, CH-8092 ZÜRICH, SWITZERLAND.

DEPARTMENT OF EARTH SCIENCES, ETH ZÜRICH, CH-8092 ZÜRICH, SWITZERLAND.